Exp.-Nr. **A2**
Eingang:
an PAC:

Mainz Microtron MAMI

A2 Collaboration at MAMI
Spokespersons: P. Pedroni, A. Thomas

Proposal for an Experiment

"High Statistics Measurement of the π^0 Transition Form Factor"

Spokespersons for the Experiment :
Patrik Adlarson (Institute for Nuclear Physics, JGU Mainz, Germany)
Achim Denig (Institute for Nuclear Physics, JGU Mainz, Germany)
Sergey Prakhov (Institute for Nuclear Physics, JGU Mainz, Germany)

Abstract of Physics :
We propose to carry out the world's most precise measurement of the time-like transition form factor (TFF) of the neutral pion by analyzing a data sample of $2.4 \cdot 10^6$ Dalitz decays, $\pi^0 \to e^+e^-\gamma$. The goal is to measure the slope parameter a_π of the π^0 TFF with an accuracy of 0.004, the current PDG average. The PDG value is dominated by TFF data in the space-like region at relatively high Q^2 from which an extrapolation is made. A direct measurement at low Q^2, as proposed here, is highly motivated by the relation of the TFF to the hadronic light-by-light contribution of the anomalous magnetic moment of the muon, $(g-2)_\mu$. This is therefore a high-accuracy test of the Standard Model. As additional spin-off analyses, we can also search for Dark Photons in the e^+e^- invariant mass spectrum and perform a feasibility study for axion searches in the $\gamma\gamma$ final state.

Abstract of Equipment :
The experiment will be performed at the tagged photon facility of MAMI (Glasgow Tagger) by using the Crystal-Ball/TAPS detector setup together with particle identification detector (PID).

MAMI Specifications :

beam energy	855 MeV
beam polarization	unpolarized

Photon Beam Specifications :

tagged energy range	140 – 798 MeV
photon beam polarization	unpolarized

Equipment Specifications :

detectors	Crystal Ball, TAPS, PID
target	liquid hydrogen, 10 cm long

Beam Time Request :

set-up/test with beam	24 hours
data taking LH_2 + empty target	600 + 50 hours

List of participating authors :
University of Massachusetts, Amherst, Massachusetts, USA
R. Miskimen, A. Rajabi
Institut für Physik, University of Basel, Basel, Switzerland
M. Dieterle, S. Garni, A. Kaeser, B. Krusche, M. Oberle, Th. Strub, N. Walford, L. Witthauer
Helmholtz-Institut für Strahlen- und Kernphysik, University of Bonn, Bonn, Germany
F. Afzal, R. Beck, K. Spieker, A. Thiel
Joint Institute for Nuclear Research, Dubna, Russia
N. S. Borisov, A. Lazarev, A. Neganov, Yu. A. Usov
School of Physics, University of Edinburgh, Edinburgh, United Kingdom
D. Glowa, S. Kay, D. P. Watts, L. A. Zana
SUPA School of Physics and Astronomy, University of Glasgow, Glasgow, United Kingdom
J. R. M. Annand, S. Gardner, D. I. Glazier, K. Livingston, I. J. D. MacGregor, C. Mullen, J. Robinson, G. Rosner, B. Strandberg, D. Werthmüller
Saint Marys University, Halifax, Nova Scotia, Canada
C. Collicott, **Racah Institute of Physics, Hebrew University of Jerusalem, Jerusalem, Israel**
G. Ron
Kent State University, Kent, Ohio, USA
D. M. Manley
Institut für Kernphysik, University of Mainz, Mainz,Germany
P. Adlarson, H. J. Arends, M. Biroth, F. Cividini, A. Denig, P. Drexler,M. I. Ferretti Bondy, W. Gradl, O. Jahn, V. L. Kashevarov, J. Linturi, P. P. Martel, A. Neiser, M. Ostrick, S. Prakhov, C. Sfienti, V. Sokhoyan, O. Steffen, M. Thiel, A. Thomas, S. Wagner, J. Wettig, M. Wolfes
Institute for Theoretical and Experimental Physics, SRC Kurchatov Institute, Moscow, Russia
V. V. Kulikov, M. Martemianov
INFN Sezione di Pavia, Pavia, Italy
A. Braghieri, S. Costanza, P. Pedroni
University of Regina, Regina, Saskatchewan, Canada
Z. Ahmed, G. M. Huber, D. Paudyal
Mount Allison University, Sackville, New Brunswick, Canada
D. Hornidge
The George Washington University, Washington, DC, USA
W. J. Briscoe, E. J. Downie, I. I. Strakovsky
Rudjer Boskovic Institute, Zagreb, Croatia
M. Korolija, I. Supek

1 Scientific background and motivation

The electromagnetic (e/m) transition form factors (TFFs) of light mesons play an important role in understanding the properties of these particles as well as in low-energy precision tests of the Standard Model (SM) and Quantum Chromodynamics (QCD) [1]. In particular, these TFFs enter as contributions to the hadronic light-by-light (HLbL) scattering calculations [2, 3] that are important for more accurate theoretical determinations of the anomalous magnetic moment of the muon, $(g-2)_\mu$, within the SM (see Refs. [4,5]). Recently, data-driven approaches, which uses dispersion relations, have been proposed [2,3,6] to make a substantial and model-independent impact on a better determination of the HLbL contribution to $(g-2)_\mu$. The precision of the calculations used to describe the HLbL calculation of $(g-2)_\mu$ can then be tested by directly comparing theoretical predictions of these approaches for e/m TFFs of light mesons with experimental data.

The TFF parameters that can be extracted from the Dalitz decay of the lightest meson, $\pi^0 \to e^+e^-\gamma$, are important to constrain calculations that estimate the pion-exchange term, $a_\mu^{\pi^0}$, to the HLbL scattering contribution to $(g-2)_\mu$. The precise knowledge of the π^0 TFF is essential for a precision calculation of the $\pi^0 \to e^+e^-$ decay rate [7,8]. In addition, the π^0 Dalitz decay has lately attracted special attention in searches of a hypothetical dark photon, U, that could be looked for via the decay chain $\pi^0 \to U\gamma \to e^+e^-\gamma$ [9].

For a structureless (pointlike) meson A, its decay into a lepton pair plus a photon, $A \to l^+l^-\gamma$, can be described within Quantum Electrodynamics (QED) via $A \to \gamma^*\gamma$, with the virtual photon γ^* decaying into the lepton pair [10]. For the meson A, QED predicts a specific strong dependence of its decay rate on the dilepton invariant mass, $m_{ll} = q$. A deviation from the pure QED dependence, caused by the actual electromagnetic structure of the meson A, is formally described by its e/m TFF [11]. The Vector-Meson-Dominance (VMD) model [12] can be used to describe the coupling of the virtual photon γ^* to the meson A via an intermediate virtual vector meson V. This mechanism is especially strong in the timelike (the energy transfer larger than the momentum transfer) momentum-transfer region, $(2m_l)^2 < q^2 < m_A^2$, where a resonant behavior near momentum transfer $q^2 = m_V^2$ of the virtual photon arises because the virtual vector meson is approaching the mass shell [11], or even reaching it, as it is in the case of the $\eta' \to l^+l^-\gamma$ decay. Experimentally, timelike TFFs can be determined by measuring the actual decay rate of $A \to l^+l^-\gamma$ as a function of the dilepton invariant mass $m_{ll} = q$, normalizing this dependence to the partial decay width $\Gamma(A \to \gamma\gamma)$, and then taking the ratio to the pure QED dependence for the decay rate of $A \to \gamma^*\gamma \to l^+l^-\gamma$.

Due to the low π^0 mass, the virtual photon γ^* in the Dalitz decay of π^0 can produce only the lightest lepton pair, e^+e^-, with $m_{ee} = q$. Based on QED, the decay rate of $\pi^0 \to \gamma^*\gamma \to e^+e^-\gamma$ can be parametrized as [11]

$$\begin{aligned} & \frac{d\Gamma(\pi^0 \to e^+e^-\gamma)}{dm_{ee}\Gamma(\pi^0 \to \gamma\gamma)} = \frac{4\alpha}{3\pi m_{ee}} \times \\ \times \quad & (1-\frac{4m_e^2}{m_{ee}^2})^{\frac{1}{2}}(1+\frac{2m_e^2}{m_{ee}^2})(1-\frac{m_{ee}^2}{m_{\pi^0}^2})^3|F_{\pi^0\gamma}(m_{ee})|^2 = \\ = \quad & [\mathrm{QED}(m_{ee})]|F_{\pi^0\gamma}(m_{ee})|^2, \end{aligned} \tag{1}$$

where $F_{\pi^0\gamma}$ is the TFF of the π^0 meson, m_{π^0} and m_e are the masses of the π^0 meson and $e^{+/-}$, respectively. Because of the smallness of the momentum-transfer range for the

$\pi^0 \to e^+e^-\gamma$ decay, its TFF is typically parametrized as [13]

$$F_{\pi^0\gamma}(m_{ee}) = 1 + a_\pi \frac{m_{ee}^2}{m_{\pi^0}^2}, \tag{2}$$

where the parameter a_π reflects the TFF slope at $m_{ee} = 0$. A simple VMD model incorporates only the ρ, ω, and ϕ resonances (in the narrow-width approximation) as virtual vector mesons driving the photon interaction in $A \to \gamma^*\gamma$. Using a quark model for the correspondent couplings leads to neglecting ϕ and yields [11] $a_\pi/m_{\pi^0}^2 = 0.5(1+m_\rho^2/m_\omega^2)/m_\rho^2 \approx 1.648$ GeV^{-2} (or $a_\pi \approx 0.0300$) for the π^0 Dalitz decay. A more modern VMD prediction, also including the ϕ-meson contribution, leads to $a_\pi \approx 0.0305$ [14].

Another feature of the decay amplitude is an angular anisotropy of the virtual photon decaying into the e^+e^- pair, which also determines the density of events along $m^2(\gamma e^{+/-})$ of the $\pi^0 \to e^+e^-\gamma$ Dalitz decay. For the e^+, e^-, and γ in the π^0 rest frame, the angle θ^* between the direction of one of the leptons in the virtual-photon (or the dilepton) rest frame and the direction of the dilepton system (which is opposite to the γ direction) follows the dependence [15]:

$$f(\cos\theta^*) = 1 + \cos^2\theta^* + (\frac{2m_e}{m_{ee}})^2 \sin^2\theta^*, \tag{3}$$

with the $\sin^2\theta^*$ term becoming very small when $m_{ee} >> 2m_e$.

Both the [QED(m_{ee})] term in Eq. (1) and the angular dependence in Eq. (3) represent only the leading-order term of the $\pi^0 \to e^+e^-\gamma$ decay amplitude, which needs radiative corrections for a more accurate calculation of [QED($m_{ee}, \cos\theta^*$)]. The most recent calculations of radiative corrections to the differential decay rate of the Dalitz decay $\pi^0 \to e^+e^-\gamma$ were reported in Ref. [16], recalculating the Mikaelian and Smith radiative corrections [17] beyond the soft-photon approximation. Typically radiative corrections makes the angular dependence of the virtual-photon decay more shallow. For the π^0 Dalitz decay, the corrected [QED] term integrated over $\cos\theta^*$ is $\sim 1\%$ larger than the leading-order term at $q = 15$ MeV and becomes $\sim 10\%$ lower at $q = 120$ MeV.

Despite the existence of recent high-statistics experiments searching for a dark-photon signal in $\pi^0 \to e^+e^-\gamma$ decays [18–20], the magnitude of the Dalitz-decay slope parameter a_π and its uncertainty in the Review of Particle Physics (RPP) [13], $a_\pi = 0.032 \pm 0.004$, are most precisely determined by a measurement of CLEO of the spacelike TFF of the π^0 meson in the process $e^+e^- \to e^+e^-\pi^0$. Extrapolating this spacelike TFF under the assumption of the validity of VMD, the following value of a_π has been extrapolated:
$a_\pi = 0.0326 \pm 0.0026_{\rm stat} \pm 0.0026_{\rm syst}$.
It should be noted, however, that this result does not only introduce a certain model dependence, but furthermore requires an extrapolation from the range of momentum transfers above 0.5 GeV^2, where the actual measurement took place, towards small momentum transfers.
The most accurate value of the slope parameter obtained from the π^0 Dalitz decay, $a_\pi = 0.025 \pm 0.014_{\rm stat} \pm 0.026_{\rm syst}$ [22], is based on the analysis of $54 \cdot 10^3$ events, with radiative corrections according to Ref. [17]. This result does not provide any $|F_{\pi^0\gamma}(m_{ee})|^2$ data points.

Recent theoretical calculations for the $\pi^0 \to \gamma^*\gamma \to e^+e^-\gamma$ TFF, in addition to the slope parameter a_π, also involve the curvature parameter b_π:

$$F_{\pi^0\gamma}(m_{ee}) = 1 + a_\pi \frac{m_{ee}^2}{m_{\pi^0}^2} + b_\pi \frac{m_{ee}^4}{m_{\pi^0}^4} \ . \tag{4}$$

The calculation based on a model-independent method using Padé approximants was reported in Ref. [23]. The analysis of spacelike data (CELLO [21], CLEO [24], BABAR [25], and Belle [26]) with this method provides a good and systematic description of the low energy region, resulting in $a_\pi = 0.0324 \pm 0.0012_{\rm stat} \pm 0.0019_{\rm syst}$ and $b_\pi = (1.06 \pm 0.09_{\rm stat} \pm 0.25_{\rm syst}) \cdot 10^{-3}$. Even more precise values, $a_\pi = 0.0307 \pm 0.0006$ and $b_\pi = (1.10 \pm 0.02) \cdot 10^{-3}$, were recently obtained by using dispersion theory [14]. In that analysis, the singly-virtual TFF was calculated in both the timelike and the spacelike regions, based on data for the $e^+e^- \to 3\pi$ cross section, generalizing previous studies on $\omega/\phi \to 3\pi$ decays [27] and $\gamma\pi \to \pi\pi$ scattering [28], and verifying the results by comparing them to timelike $e^+e^- \to \pi^0\gamma$ data at large momentum transfer.

The capability of the A2 experimental setup to measure Dalitz decays was demonstrated in Refs. [29, 30] for $\eta \to e^+e^-\gamma$. Measuring $\pi^0 \to e^+e^-\gamma$ is challenging because of the smallness of the TFF effect in the region of very low momentum transfer; the magnitude of $|F_{\pi^0\gamma}|^2$ is expected to reach only a 5% enhancement above the pure QED dependence at $m_{ee} = 120$ MeV/c^2. Thus, such a measurement requires high statistics to reach a statistical accuracy comparable with the expected TFF effect. Also, the magnitude of systematic uncertainties caused by the acceptance determination, background subtraction, and experimental resolutions should be small. The advantage of measuring $\pi^0 \to e^+e^-\gamma$ with the A2 setup at MAMI is that π^0 mesons can be produced in the reaction $\gamma p \to \pi^0 p$ which has a very large cross section at the energies close the $\Delta(1232)$ state, and there is no background from other physical reactions at these energies. The only background for $\pi^0 \to e^+e^-\gamma$ decays are $\pi^0 \to \gamma\gamma$ decays with a photon converting into an e^+e^- pair in the material in front of electromagnetic calorimeters.

In this proposal, the capability of the A2 experimental setup to measure the e/m TFF of π^0 is demonstrated with the results obtained from a total of $\sim 4 \cdot 10^5$ $\pi^0 \to e^+e^-\gamma$ decays detected in the previous A2 experiments dedicated to measuring the $\gamma p \to \pi^0 p$ reaction [31, 32].

2 Experimental setup

The process $\gamma p \to \pi^0 p \to e^+e^-\gamma p$ will be measured by using the Crystal Ball (CB) [33] as a central calorimeter and TAPS [34, 35] as a forward calorimeter. These detectors are installed in the energy-tagged bremsstrahlung photon beam of the Mainz Microtron (MAMI) [36,37]. The photon energies are determined by using the Glasgow–Mainz tagging spectrometer [38–40].

The CB detector is a sphere consisting of 672 optically isolated NaI(Tl) crystals, shaped as truncated triangular pyramids, which point toward the center of the sphere. The crystals are arranged in two hemispheres that cover 93% of 4π, sitting outside a central spherical cavity with a radius of 25 cm, which holds the target and inner detectors. In the A2 experiments at MAMI-C (after 2006), TAPS was initially arranged in a plane consisting of 384 BaF_2 counters of hexagonal cross section. It was installed 1.5 m

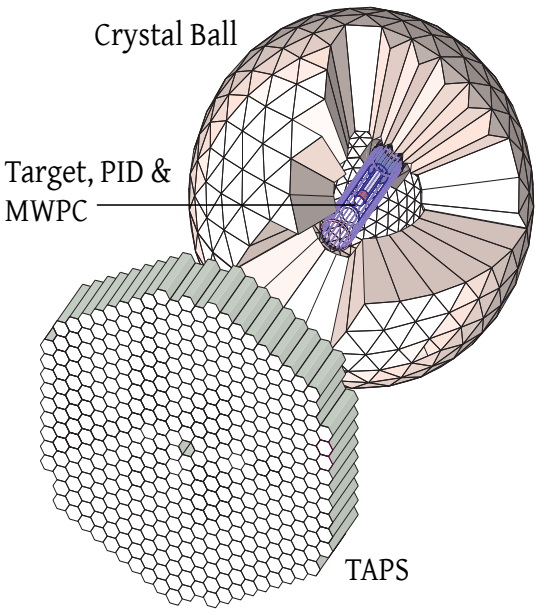

Figure 1: (Color online) A general sketch of the Crystal Ball, TAPS, and particle identification (PID) detectors.

downstream of the CB center and covered the full azimuthal range for polar angles from 1° to 20°. In the present experiments, 18 BaF_2 crystals, covering polar angles from 1° to 5°, were replaced with 72 $PbWO_4$ crystals. This allowed running with a much higher MAMI electron current, without decreasing the TAPS efficiency due to the very high count rate in the crystals near the photon-beam line. More details on the energy and angular resolution of the CB and TAPS are given in Refs. [41, 42].

The proposed measurement will use electron beam with energy 855 MeV from the Mainz Microtron, MAMI-C [37]. The A2 data that were used to check the capability of the present experimental setup for measuring the π^0 TFF were taken with the 855-MeV (Run-I) [31] and with the 1557-MeV beam (Run-II) [32]. Bremsstrahlung photons, produced by the beam electrons in a radiator (10-μm Cu to be used) and collimated by a Pb collimator (with diameter 4 mm), will be incident on a 10-cm-long liquid hydrogen (LH_2) target located in the center of the CB. The total amount of the material around the LH_2 target, including the Kapton cell and the 1-mm-thick carbon-fiber beamline, is equivalent to 0.8% of a radiation length X_0. In the present measurement, it is essential to keep the material budget as low as possible to minimize the $\pi^0 \to \gamma\gamma$ background with conversion of real photons into e^+e^- pairs.

The target is surrounded by a Particle IDentification (PID) detector [44] used to distinguish between charged and neutral particles. It is made of 24 scintillator bars (50 cm long, 4 mm thick) arranged as a cylinder with a radius of 12 cm. A general sketch of the CB, TAPS, and PID is shown in Fig. 1. A multi-wire proportional chamber (MWPC), also shown in this figure, is not planned to be used in the data analysis because of its comparably lower efficiency for detecting $e^{+/-}$.

The energies of the incident photons will be analyzed from 140 up to 798 MeV by detecting the postbremsstrahlung electrons in the Glasgow tagged-photon spectrometer (Glasgow tagger) [38–40]. The uncertainty in the energy of the tagged photons is mainly determined by the number of tagger focal-plane detectors in combination with the energy

of the MAMI electron beam used in the experiments. Increasing the MAMI energy increases the energy range covered by the spectrometer and also has the corresponding effect on the uncertainty in E_γ. For the MAMI energy settings of 855 MeV, this uncertainty is about ± 1 MeV. More details on the tagger energy calibration and uncertainties in the energies can be found in Ref. [43].

The experimental trigger will require the total energy deposited in the CB to exceed $\sim$140 MeV, without involving any multiplicity trigger. Such a choice is based on the necessity to detect all particles from π^0 decays inside the CB, which is covered by the PID needed for separating leptons from photons. Because photoproduction of π^0 dominates by the first resonant region, the total energy deposited from the π^0 decay products will be somewhat higher than the π^0 mass. Energies of some e^+, e^-, and γ from π^0 decays could go to very low values, which will be below the multiplicity-trigger threshold. Such a trigger will be also efficient for detecting $\pi^0 \to \gamma\gamma$ decays, needed for the $\pi^0 \to e^+e^-\gamma$ normalization and for generating the $\gamma p \to \pi^0 p$ reaction in the Monte Carlo simulation according to the actual spectra, measured in the same experiment.

3 Experimental procedure

3.1 Event selection

To search for a signal from $\pi^0 \to e^+e^-\gamma$ decays, candidates for the process $\gamma p \to e^+e^-\gamma p$ will be extracted from the analysis of events having three and four clusters reconstructed in the CB and TAPS together by software analysis. The offline cluster algorithm is optimized for finding a group of adjacent crystals in which the energy was deposited by a single-photon e/m shower. This algorithm also works well for $e^{+/-}$ and proton clusters. For the $\gamma p \to e^+e^-\gamma p$ candidates, the three-cluster events are analyzed assuming that the final-state proton was not detected. To diminish possible background from $\gamma p \to \pi^0\pi^0 p$ and $\gamma p \to \pi^0\pi^+ n$, the selected energy range will be limited to $E_\gamma < 450$ MeV, corresponding to the largest π^0 cross sections.

The selection of candidate events and the reconstruction of the reaction kinematics will be based on the kinematic-fit technique. Details of the kinematic-fit parametrization of the detector information and resolutions are given in Ref. [41]. Because e/m showers from electrons and positrons are very similar to those of photons, the hypothesis $\gamma p \to 3\gamma p$ is tested to identify the $\gamma p \to e^+e^-\gamma p$ candidates. The events that satisfied this hypothesis with the CL greater than 1% are accepted for further analysis. The kinematic-fit output is used to reconstruct the kinematics of the outgoing particles. In this output, there is no separation between e/m showers caused by the outgoing photon, electron, or positron. Because the main purpose of the experiment is in measuring the $\pi^0 \to e^+e^-\gamma$ decay rate as a function of the invariant mass $m(e^+e^-)$, the next step in the analysis is the separation of the e^+e^- pair from the final-state photon. This procedure is optimized by using a Monte Carlo (MC) simulation of the process $\gamma p \to \pi^0 p \to e^+e^-\gamma p$.

3.2 Monte Carlo simulations

Because of the limited experimental resolution in the invariant mass $m(e^+e^-)$ ($\sigma_m \approx$ 5.7 MeV) and the detection threshold for particles in the experimental setup, the MC simulation has to be made to be as similar as possible to the real $\gamma p \to \pi^0 p \to e^+e^-\gamma p$

events. This was important for minimizing systematic uncertainties in the determination of experimental acceptances and proper measuring the TFF energy dependence. To reproduce the experimental yield of π^0 mesons and their angular distributions as a function of the incident-photon energy, the $\gamma p \to \pi^0 p$ reaction is generated according to the numbers of the corresponding π^0 events and their angular distributions measured in the same experiment. The $\pi^0 \to e^+e^-\gamma$ decay is generated according to Eq. (1) with the phase-space term removed and with $a_\pi = 0.032$ from RPP [13] for the TFF dependence. The angular dependence of the virtual photon decaying into the e^+e^- pair is generated according to Eq. (3). Then these dependences from the leading-order QED term of the decay amplitude are convoluted with radiative corrections based on the calculations of Ref. [16]. The event vertices are generated uniformly along the 10-cm-long LH_2 target.

The main background process, $\gamma p \to \pi^0 p \to \gamma\gamma p$, is also studied by using its MC simulation. The yield and the production angular distributions of $\gamma p \to \pi^0 p$ are generated in the same way as for the process $\gamma p \to \pi^0 p \to e^+e^-\gamma p$.

For both π^0 decay modes, the generated events are propagated through a GEANT (version 3.21) simulation of the experimental setup. To reproduce resolutions of the experimental data, the GEANT output (energy and timing) is subject to additional smearing, thus allowing both the simulated and experimental data to be analyzed in the same way. Matching the energy resolution between the experimental and MC events is achieved by adjusting the invariant-mass resolutions, the kinematic-fit stretch functions (or pulls), and probability distributions. Such an adjustment is based on the analysis of the same data sets for the reaction $\gamma p \to \pi^0 p \to \gamma\gamma p$, having almost no background from other physical reactions at these energies. The simulated events are also tested to check whether they passed the trigger requirements.

3.3 $e^{+/-}$ identification and background suppression

The PID detector is used to identify the final-state e^+e^- pair (the detection efficiency for $e^{+/-}$ passed through the PID is close to 100%) in the events selected as $\gamma p \to 3\gamma p$ candidates. Because, with respect to the LH_2 target, the PID provides a full coverage only for the CB crystals, only events with three e/m showers in the CB are selected for further analysis. This also makes all selected events pass the trigger requirement on the total energy in the CB. The identification of $e^{+/-}$ in the CB is based on a correlation between the ϕ angles of fired PID elements with the angles of e/m showers in the calorimeter. The MC simulation of $\gamma p \to \pi^0 p \to e^+e^-\gamma p$ is used to optimize this procedure, minimizing a probability of misidentification of $e^{+/-}$ with the final-state photons. This procedure is optimized how close an e/m shower in the CB should be to a fired PID element to be considered as $e^{+/-}$, and how far it should be to be considered as a photon. It is causing some inefficiency in true events for which the ϕ angle of the electron or the positron is close to the photon ϕ angle.

The analysis of the MC simulation for the main background reaction $\gamma p \to \pi^0 p \to \gamma\gamma p$ reveals that this process can mimic $\pi^0 \to e^+e^-\gamma$ events when one of the final-state photons converts into an e^+e^- pair in the material between the production vertex and the NaI(Tl) surface. Because the opening angle between such electrons and positrons is typically very small, this background contributes mostly to low invariant masses $m(e^+e^-)$. A significant suppression of this background can be reached by requiring that e^+ and e^- are identified by different PID elements. However, such a requirement also decreases the detection

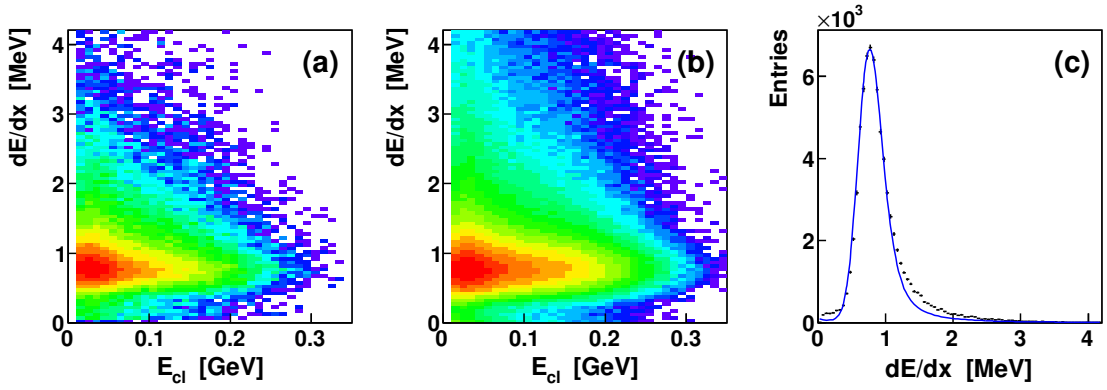

Figure 2: (Color online) Comparison of the $e^{+/-}$ dE/dx of the PID for experimental $\pi^0 \to e^+e^-\gamma$ decays and their MC simulation. The two-dimensional density distribution (with logarithmic scale along plot axis z) for the $e^{+/-}$ dE/dx of the PID versus the energy of the correspondent clusters in the CB is shown in (a) for the data and in (b) for the MC simulation. The $e^{+/-}$ dE/dx distributions for the data (crosses) and the MC simulation (blue solid line) are compared in (c).

efficiency for good $\pi^0 \to e^+e^-\gamma$ events, especially at low invariant masses $m(e^+e^-)$. In further analysis of $\pi^0 \to e^+e^-\gamma$ events, both options, with larger and smaller background remaining from $\pi^0 \to \gamma\gamma$, can be tested.

The background source from $\gamma p \to \pi^0 p \to \gamma\gamma p$ occurs when one photon deposits some energy in the PID, then its e/m shower, together with the recoil proton, could be misidentified as an e^+e^- pair. Such background does not mimic the $\pi^0 \to e^+e^-\gamma$ peak, but the suppression of this background is improving the signal-to-background ratio, which is important for more reliable fitting the signal peak above the remaining background. Similar background can come from the $\gamma p \to \pi^0 p \to e^+e^-\gamma p$ events themselves when one of the leptons failed to be detected, and the recoil proton was misidentified with this lepton. The background from the misidentification of the recoil proton with $e^{+/-}$ can be suppressed by the analysis of energy losses, dE/dx, in the PID elements. To reflect the actual differential energy deposit dE/dx in the PID, the energy signal from each elements, ascribed to either e^+ or e^-, is multiplied by $\sin(\theta)$ of the polar angle of the corresponding particle, the magnitide of which is taken from the kinematic-fit output. All PID elements are calibrated in the data to have the position of their peaks from $e^{+/-}$ at the maximum of the corresponding peak in the MC simulation. To reproduce the actual energy resolution of the PID with its MC simulation, the GEANT output for PID energies is subject to additional smearing, allowing the $e^{+/-}$ selection with dE/dx cuts to be very similar for the data and MC. The PID energy resolution in the MC simulations is adjusted to match the experimental dE/dx spectra for the $e^{+/-}$ particles from $\pi^0 \to e^+e^-\gamma$ decays observed experimentally. Possible systematic uncertainties due to applying dE/dx cuts can be checked via the stability of the results after narrowing the dE/dx range for selecting $e^{+/-}$.

The experimental dE/dx resolution of the PID for $e^{+/-}$ and the comparison of it with its MC simulation is illustrated in Fig. 2. Figures 2(a) and (b) show (for the data and the MC simulation, respectively) two-dimensional plots of the $e^{+/-}$ dE/dx of the PID versus the energy of the correspondent clusters in the CB. As seen, there is no dE/dx

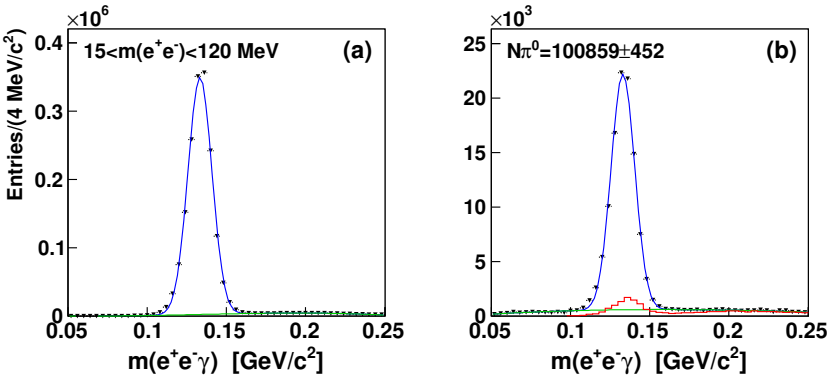

Figure 3: (Color online) $m(e^+e^-\gamma)$ invariant-mass distributions obtained in the analysis of Run-I for the $m(e^+e^-)$ range from 15 to 120 MeV/c^2 with $\gamma p \to e^+e^-\gamma p$ candidates selected with the kinematic-fit CL>1%, a dE/dx PID cut accepting the entire range with deposits from $e^{+/-}$, and allowing both e^+ and e^- to be identified with the same PID element: (a) MC simulation of $\gamma p \to \pi^0 p \to e^+e^-\gamma p$ (black dots) fitted with the sum of a Gaussian (blue line) for the actual $\pi^0 \to e^+e^-\gamma$ peak and a polynomial (green line) of order four for the background from misidentifying the recoil proton with either e^+ or e^-; (b) experimental spectrum (black dots) after subtracting the background remaining from $\gamma p \to \pi^0 p \to \gamma\gamma p$. The $\pi^0 \to \gamma\gamma$ background, which is shown by a red line, is normalized to the number of subtracted events. The experimental distribution is fitted with the sum of a Gaussian (blue line) for the $\pi^0 \to e^+e^-\gamma$ peak and a polynomial (green line) of order four for the background.

dependence of $e^{+/-}$ on their energy in the CB, and applying cuts just on a dE/dx value is sufficient for suppressing backgrounds caused by misidentifying protons with $e^{+/-}$. The comparison of the $e^{+/-}$ dE/dx distributions for the data and the MC simulation is depicted in Fig. 2(c). A small difference in the tails of the $e^{+/-}$ peak can mostly be explained by some background remaining in the experimental spectrum. Typical PID cuts, which were tested, vary from requiring $dE/dx < 3.7$ MeV to $dE/dx < 2.7$ MeV to suppress background events, showing no systematics in the final results due to such cuts.

In addition to the background contributions discussed above, there are two more background sources. The first source comes from interactions of incident photons in the windows of the target cell. The subtraction of this background is based on the analysis of data samples that are taken with an empty (no liquid hydrogen) target. Another background is caused by random coincidences of the tagger counts with the experimental trigger; its subtraction is carried out by using event samples for which all coincidences are random.

3.4 Analysis of $\pi^0 \to e^+e^-\gamma$ decays

To measure the $\pi^0 \to e^+e^-\gamma$ yield as a function of the invariant mass $m(e^+e^-)$, the selected candidate events are divided into several $m(e^+e^-)$ bins. Events with $m(e^+e^-) <$ 15 MeV/c^2 are difficult to analyze with the present setup, because e/m showers from those e^+ and e^- start to overlap too much in the CB. The number of $\pi^0 \to e^+e^-\gamma$ decays in every $m(e^+e^-)$ bin is determined by fitting the experimental $m(e^+e^-\gamma)$ spectra with the π^0 peak rising above a smooth background.

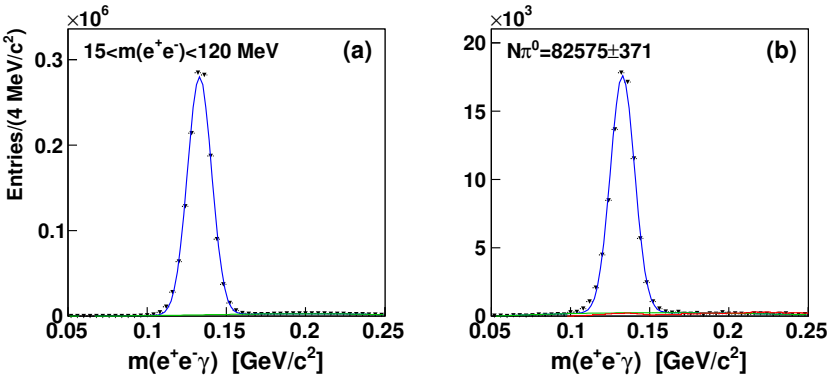

Figure 4: (Color online) Same as Fig. 3, but requiring both e^+ and e^- to be identified by different PID elements.

The fitting procedure for $\pi^0 \to e^+e^-\gamma$ and the impact of selection criteria on the background is illustrated in Figs. 3 and 4 from the analysis of Run-I, the experimental conditions which are most similar to the proposed experiment. Figure 3 shows all $\gamma p \to e^+e^-\gamma p$ candidates from Run-I in the $m(e^+e^-)$ range from 15 to 120 MeV/c^2, which were selected with the kinematic-fit CL>1%, a dE/dx PID cut accepting the entire range with deposits from $e^{+/-}$, and also allowing both e^+ and e^- to be identified with the same PID element. Figure 3(a) depicts the $m(e^+e^-\gamma)$ invariant-mass distribution for the MC simulation of $\gamma p \to \pi^0 p \to e^+e^-\gamma p$ fitted with the sum of a Gaussian for the actual $\pi^0 \to e^+e^-\gamma$ peak and a polynomial of order four for own background from misidentifying the recoil proton with either e^+ or e^-. As seen, the own background is very small, especially after the dE/dx PID cut. The experimental distribution after subtracting the random and empty-target backgrounds and the background remaining from $\gamma p \to \pi^0 p \to \gamma\gamma p$ is shown by black points in Fig. 3(b). The distribution for the $\pi^0 \to \gamma\gamma$ background is normalized to the number of subtracted events and is shown in the same figure by a red solid line. The subtraction normalization is based on the number of events generated for $\gamma p \to \pi^0 p \to \gamma\gamma p$ and the number of $\gamma p \to \pi^0 p$ events produced in the same experiment. The experimental distribution is fitted with the sum of a Gaussian for the $\pi^0 \to e^+e^-\gamma$ peak and a polynomial of order four for the background. The centroid and width of the Gaussian obtained in both the fits (to the MC-simulation and experimental spectra) are in good agreement with each other. This confirms the agreement of the experimental data and the MC simulation in the energy calibration of the calorimeters and their resolution. The order of the polynomial is chosen to be sufficient for a fairly good description of the background distribution in the range of fitting.

The number of $\pi^0 \to e^+e^-\gamma$ decays in both the MC-simulation and the experimental $m(e^+e^-\gamma)$ spectra is determined from the area under the Gaussian. For the selection criteria and the $m(e^+e^-)$ range used to obtain the spectra in Fig. 3, the averaged detection efficiency is determined to be 23.2%.

Figure 4 illustrates the effect of requiring both e^+ and e^- to be identified by different PID elements. As seen, compared to Fig. 3(b), the level of background contributions, including $\pi^0 \to \gamma\gamma$, under the $\pi^0 \to e^+e^-\gamma$ peak becomes very small, whereas the average detection efficiency decreases to 18.7%. The results for the $\pi^0 \to e^+e^-\gamma$ yield obtained with and without adding events with e^+ and e^- identified by the same PID element show

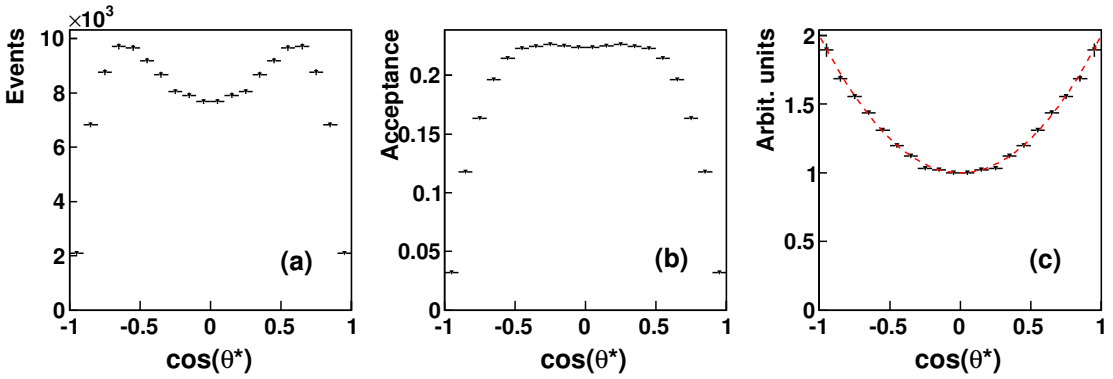

Figure 5: (Color online) The $\pi^0 \to \gamma\gamma^* \to \gamma e^+e^-$ angular dependence (in the π^0 rest frame) of the virtual photon decaying into a e^+e^- pair, with θ^* being the angle between the direction of one of the leptons in the virtual-photon (or the dilepton) rest frame and the direction of the dilepton system (which is opposite to the γ direction): (a) experimental events from the $\pi^0 \to \gamma e^+e^-$ peak; (b) angular acceptance based on the MC simulation; (c) the experimental spectrum corrected for the acceptance and normalized for comparing to the $1 + \cos^2\theta^*$ dependence (shown by a red dashed line).

good agreement within the fit uncertainties, confirming the reliability in the subtraction of the remaining $\pi^0 \to \gamma\gamma$ background.

Requiring both e^+ and e^- to be identified by different PID elements results in almost full elimination of the background contributions under the $\pi^0 \to e^+e^-\gamma$ peak. This enables measuring the $\pi^0 \to \gamma\gamma^* \to \gamma e^+e^-$ angular dependence of the virtual photon decaying into an e^+e^- pair and comparing it with Eq. (3). The experimental results for such an angular dependence are illustrated in Fig. 5 for events from the $\pi^0 \to e^+e^-\gamma$ peak of Run-I. Figure 5(a) shows the experimental $\cos\theta^*$ distribution. The angular acceptance determined from the MC simulation is depicted in Fig. 5(b). The experimental distribution corrected for the acceptance is depicted in Fig. 5(c), showing good agreement with the expected $1 + \cos^2\theta^*$ dependence, the averaged distortion of which due to radiative corrections is quite small. Because e^+ and e^- cannot be separated in the present experiment, the angles of both leptons were used to measure the dilepton decay dependence, which resulted in a symmetric shape with respect to $\cos\theta^* = 0$.

The statistics available for Run-I and Run-II and the level of background for $\pi^0 \to e^+e^-\gamma$ decays enable to divide all candidate events into 18 bins, covering the $m(e^+e^-)$ range from 15 to 120 MeV/c^2. The bins are 5 MeV wide up to 90 MeV/c^2, and 10 MeV wide above it. Fits to the spectra were made separately for Run-I and Run-II, and the final results were combined together as independent measurements. The fitting procedure was the same as shown in Figs. 3 and 4.

4 Measuring the π^0 TFF

The total number of $\pi^0 \to e^+e^-\gamma$ decays initially produced in each $m(e^+e^-)$ bin is obtained by correcting the number of decays observed in this bin with the corresponding detection efficiency. The results for $|F_{\pi^0\gamma}(m_{e^+e^-})|^2$ are obtained from those initial numbers of decays by taking into account the total number of π^0 mesons produced in the same data

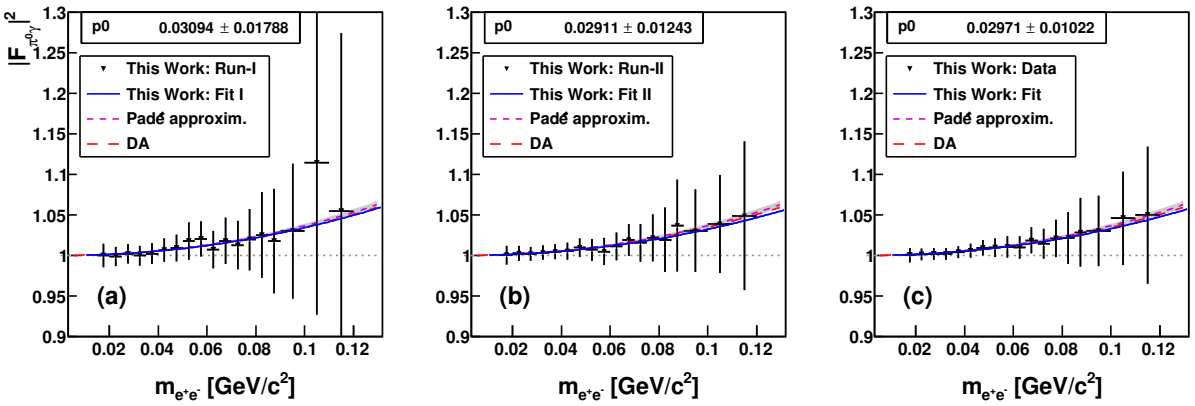

Figure 6: (Color online) $|F_{\pi^0\gamma}|^2$ results (black filled triangles) obtained from Run-I (a), Run-II (b), and the combined values (c) are fitted with Eq. (2) (shown by blue lines, with $p0$ being the slope parameter a_π) and compared to the calculations with Padé approximants [23] (shown by a short-dashed magenta line with an error band) and to the dispersive analysis (DA) from Ref. [14] (long-dashed red line). The error band for the latter analysis is by a factor of four narrower, compared to the shown, and is omitted because of its smallness. The error bars on all data points represent the total uncertainties of the results.

sets [31, 32], the $\pi^0 \to \gamma\gamma$ branching ratio from RPP [13], and the [QED(m_{ee})] term from Eq. (1) corrected for radiative corrections according to the calculations of Ref. [16]. The uncertainty in an individual $|F_{\pi^0\gamma}(m_{e^+e^-})|^2$ value from a particular fit are based on the uncertainty in the number of decays determined by this fit. The systematic uncertainties in the $|F_{\pi^0\gamma}(m_{e^+e^-})|^2$ values are estimated for each individual $m(e^+e^-)$ bin by repeating its fitting procedure several times after refilling the spectra with different combinations of selection criteria, which are used to improve the signal-to-background ratio, and slight changes in the parametrization of the background under a signal peak. The changes in selection criteria include cuts on the kinematic-fit CL (such as 1% 2%, 5%, and 10%), different cuts on PID dE/dx, and switching on and off the requirement for both e^+ and e^- to be identified by different PID elements. Making several fits for each $m(e^+e^-)$ bin provides a check on the stability of the $|F_{\pi^0\gamma}(m_{e^+e^-})|^2$ results, the average of which is then used to obtain more reliable TFF values.

Because the fits for one $m(e^+e^-)$ bin with different selection criteria are based on the same data, the corresponding $|F_{\pi^0\gamma}(m_{e^+e^-})|^2$ results are correlated and cannot be considered as independent measurements. Then, a final $|F_{\pi^0\gamma}(m_{e^+e^-})|^2$ value for one $m(e^+e^-)$ bin is obtained by averaging the results of all fits made for this bin. The average of the corresponding $|F_{\pi^0\gamma}(m_{e^+e^-})|^2$ uncertainties, calculated from the fit errors, is considered as the fit uncertainty (partially reflecting the bin statistic) of the $|F_{\pi^0\gamma}(m_{e^+e^-})|^2$ value in this bin. The systematic uncertainty in this $|F_{\pi^0\gamma}(m_{e^+e^-})|^2$ value is taken as the root mean square of the results from all fits made for this bin. The total uncertainty in this $|F_{\pi^0\gamma}(m_{e^+e^-})|^2$ value is calculated by adding in quadrature its fit and systematic uncertainties. In the end, the $|F_{\pi^0\gamma}(m_{e^+e^-})|^2$ results from Run-I and Run-II, which were independent measurements, are combined as a weighted average with weights taken as inverse values of their total uncertainties in quadrature.

The individual $|F_{\pi^0\gamma}(m_{e^+e^-})|^2$ results obtained from Run-I, Run-II, and their weighted average are depicted in Figs. 6(a), (b), and (c), respectively. The error bars plotted on all data points represent the total uncertainties of the results. Fits of the data points with Eq. (2) are shown by blue solid lines. The fit parameter $p0$ corresponds to the slope parameter a_π. Because the fits are made to the data points with their total uncertainties, the fit errors for a_π give their total uncertainty as well. The present experimental results depicted in Fig. 6 are also compared to the calculations with Padé approximants [23] and to the dispersive analysis (DA) from Ref. [14], which were discussed earlier in the Introduction. As seen, all fits to the data points lie slightly lower than the calculations. However, the magnitude of the experimental uncertainties does not allow one to speak about any disagreement between the data and the calculations. In addition, attempts of fitting the present data points with Eq. (4) cannot provide any reliable values for the curvature parameter b_π, also resulting in strong correlation between the parameters a_π and b_π. The comparison of the individual results obtained from Run-I and Run-II illustrates their good consistency within the error bars, even though the uncertainties from Run-I are significantly larger than those from Run-II.

Based on the fit to the data points combined from Run-I and Run-II, the magnitude obtained for the slope parameter,

$$a_\pi = 0.030 \pm 0.010_{\rm tot}, \tag{5}$$

shows, within the uncertainties, good agreement with the RPP value, $a_\pi = 0.032 \pm 0.004$ [13], and with the calculations from Ref. [23], $a_\pi = 0.0324 \pm 0.0012_{\rm stat} \pm 0.0019_{\rm syst}$, and Ref. [14], $a_\pi = 0.0307 \pm 0.0006$. Though the uncertainty obtained for a_π from the analysis of Run-I and Run-II is significantly larger than the accuracy of those values, this uncertainty is smaller than in all previous measurements based on the $\pi^0 \to e^+e^-\gamma$ decay.

The comparison of the magnitudes for the fit and systematic uncertainties in the individual $|F_{\pi^0\gamma}(m_{e^+e^-})|^2$ results shows the dominance of fit uncertainties, reflecting the experimental statistics. Thus, a more precise measurement of the π^0 TFF at low momentum transfer with the Dalitz decay $\pi^0 \to e^+e^-\gamma$ needs a significant increase in experimental statistics. The π^0 TFF parameters extracted from such a precision measurement could then constrain calculations that estimate the pion-exchange term, $a_\mu^{\pi^0}$, to the HLbL scattering contribution to $(g-2)_\mu$.

5 Event Rates and Beam Time Estimation

Estimates of the counting rate are based on the analyses of the existing A2 data (Run-I and Run-II) appropriate for measuring the π^0 TFF. For the conditions of Run-II, the rate of good detected $\pi^0 \to e^+e^-\gamma$ decays was $\sim 1.1 \cdot 10^3$ per hour. Decreasing the MAMI energy to 855 MeV (which was 1557 MeV for Run-II) will decrease the DAQ trigger rate for triggering on a particular energy sum in the CB. Further decreasing the DAQ trigger rate will be reached by increasing the trigger requirement on the energy sum in the CB (which was 120 MeV for Run-II) to 140 MeV or slightly higher. It is estimated that by increasing the MAMI current (compared to Run-I and Run-II) to $\sim 55-60\%$ of the DAQ lifetime, in combination with a much faster readout system, the rate for good detected π^0 Dalitz decays can be increased by a factor of 2.5–3. An additional gain in this rate can be reached with the upgraded tagging facility, which will repair inefficient (and partially

inefficient) channels, needed for measuring incident-photon energies, and speed up the readout system.

Based on our estimates, 600 hours of pure data taking should be sufficient to measure the slope parameter a_π of the π^0 e/m TFF with an accuracy of 10%, which is slightly better than the uncertainty of the current RPP average, $a_\pi = 0.032 \pm 0.004$. Additionally, 50 hours are needed to measure the empty-target contributions. Measuring the tagging efficiency, which is less important for the present experiment, should be done just once in two days, and will take less than 20 hours.

The photon beam will be unpolarized and tagged in the energy range 140-798 MeV. The radiator is 10 μm Cu and a 4 mm diameter Pb collimator will be used.

6 Feasibility Studies Exotic Particles

As spin-off analyses one can also use the collected data in feasibility searches of Beyond Standard Model Physics (**BSM**). The BSM searches could be done for either spin-0 or spin-1 particles. Much experimental activity has been devoted to searches for the so called Dark Photon, γ' [9]. The Dark Photon would interact with the visible world via kinetic mixing with the Standard Model hypercharge. The main motivations for these searches have been for explaining an observed high energy positron excess in the galactic center and the $(g-2)_\mu$ anomaly. Searches of these hidden particles are conducted by resonance scans in e^+e^- invariant mass spectra with the exclusion limits set by the strength of the kinetic mixing parameter, ϵ^2, versus the γ'-mass. For the Dalitz decay the strength of the mixing parameter is given by [9]

$$Br(\pi^0 \to \gamma\gamma') = 2\epsilon^2 \left(1 - \frac{m_{\gamma'}^2}{m_{\pi^0}^2}\right) Br(\pi^0 \to \gamma\gamma). \tag{6}$$

The highest statistics experiment which uses the π^0 Dalitz decays as a probe comes from the NA48/2 collaboration and is based on $1.7{\cdot}10^7$ Dalitz decays, published in 2015 [18]. Their exclusion plot is shown in figure 7.

Since the NA48/2 results were published, two new theoretical papers have come, which would further motivate searches in the energy region accessible by the π^0 Dalitz decay. The first is motivated by a recent 6.8σ discrepancy reported in excited ^{8}Be nuclear decays via internal pair creation [45]. The experimental group hypothesize that the discrepancy can best be explained with a boson at a mass of 16.7 MeV. Based on this claimed discovery, a theoretical group investigates how the properties of this potential particle could be consistent together with other existing SM constraints [46]. They find that a protophobic gauge boson would best explain the available data. If this protophobic boson does exist one would see a resonance in the decay $\pi^0 \to \gamma(X \to e^+e^-)$ at 16.8 MeV. The predicted parameter space is only partly covered by NA48/2 data. For the Crystal Ball-TAPS setup this is on the lower boundary of what typically could be measured, but a feasibility study would see if one could extend searches also to lower $m_{e^+e^-}$ to be able to cover this region. The second theoretical work is inspired by the proton charged radius puzzle and the $(g-2)_\mu$ anomaly [47]. The proton charge radius puzzle concerns the fact that, when extracting the proton charge radius using electrons and muons, the measured value with muons gives a radius that deviates by more than 5 sigmas, compared to measurements

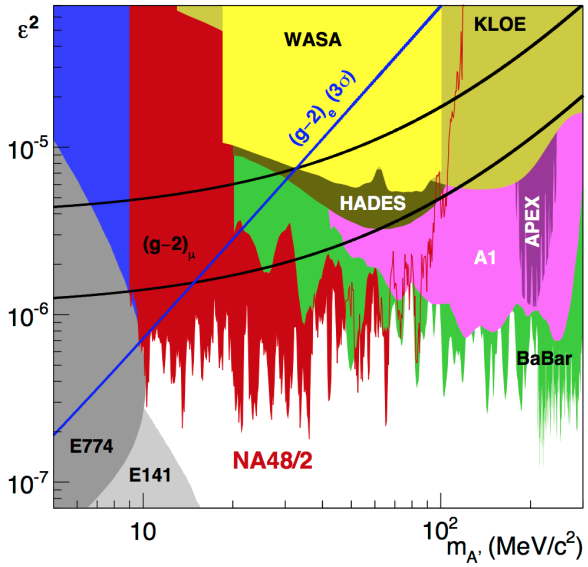

Figure 7: NA48/2 upper limits at 90% CL plot together with other experimental limits. In the NA48/2 paper γ' is called A'. Figure from [18].

with electrons. In the new regime of high precision physics, many of the fundamental constants in physics, e.g. the Rydberg constant, the fine structure constant, proton charge radius, and electron mass are intrinsically coupled. The assumption behind the theory group is that the proton charge radius puzzle and the $(g-2)_\mu$ anomaly only appear to be related to the muon for historical reasons. In their work they make a re-fit of all relevant Standard Model data with and without a BSM- boson which interacts universally with leptons and hadrons, being proportional to charge. Both hypotheses are compared with a χ^2 test. From this re-fit of data, they find new values for many of the fundamental constants of the Standard Model and, in addition, they find that the Standard Model data needs an additional particle to be able to solve current experimental discrepancies. The proposed particle could have a mass as low as 20 MeV but is also favorable for higher masses. With respect to the energy regime relevant to figure 7 and the A2 collaboration, parts of the favored band has already been excluded by many experiments. Up to 50 MeV however, only NA48/2 has excluded the relevant parameter space. This region in $m_{e^+e^-}$ could also be covered by the CB-TAPS experimental setup. Compared to the NA48/2 experiment one would be able to do an independent search with a different set of background, experimental conditions and systematics.

A third possibility to use the Dalitz decay data would be in a search for an axion-like particle motivated by the muon anomaly and electric dipole moments [48]. Although these searches are foreseen to be favorable for e^+e^- colliders and in Primakoff experiments, a feasibility study could also study the requirements needed for finding such a resonance in π^0 Dalitz decay data. In the proposed experiment, an axion can be produced via Primakoff scattering, which dominates by the very forward production angles. The axion can be searched via its decay in the two-photon final state, and in the mass range below M_η. Because the DAQ trigger will require a relatively small energy deposit in the CB ($\geq$140 MeV), without any multiplicity trigger, detecting just one photon (from an axion decay)

in the CB will be sufficient for the axion detection (with relatively good acceptance) in its mass range $\sim$15 MeV-IM$(\gamma\gamma)_{max\ allowed}$ for particular incident photon energies. The major limitations in searching for an axion signal will be if its mass is too close to M_{π^0} or M_η and the axion's life time.

It is not foreseen that one would be able to extend the exclusion limits set by NA48/2 in the experimental beam time which is proposed here. A feasibility study would, however, be able to investigate this region and, if the interest in this mass-coupling region persists, one would ask for an additional beam time, particularly motivated by BSM searches.

References

[1] E. Czerwinski, S. Eidelman, C. Hanhart, B. Kubis, A. Kupść, S. Leupold, P. Moskal, and S. Schadmand (Editors), Proceedings of *First MesonNet Workshop on Meson Transition Form Factors*, 2012, Cracow, Poland, arXiv:1207.6556 [hep-ph].

[2] G. Colangelo, M. Hoferichter, B. Kubis, M. Procura, and P. Stoffer, Phys. Lett. B **738**, 6 (2014).

[3] G. Colangelo, M. Hoferichter, M. Procura, and P. Stoffer, JHEP 1509 , 074 (2015).

[4] F. Jegerlehner and A. Nyffeler, Phys. Rep. **477**, 1 (2009).

[5] A. Nyffeler, arXiv:1602.03398 [hep-ph].

[6] V. Pauk and M. Vanderhaeghen, Phys. Rev. D **90**, 113012 (2014).

[7] T. Husek and S. Leupold, Eur. Phys. J. C **75**, 586 (2015).

[8] P. Masjuan and P. Sanchez-Puertas, arXiv:1512.09292 [hep-ph].

[9] B. Batell, M. Pospelov, and A. Ritz, Phys. Rev. D **80**, 095024 (2009).

[10] N. M. Kroll and W. Wada, Phys. Rev. **98**, 1355 (1955).

[11] L. G. Landsberg, Phys. Rep. **128**, 301 (1985).

[12] J. J. Sakurai, *Currents and mesons*, University of Chicago Press, Chicago, USA, 1969.

[13] K. A. Olive *et al.*, (Particle Data Group), Chin. Phys. C **38**, 090001 (2014).

[14] M. Hoferichter, B. Kubis, S. Leupold, F. Niecknig, and S. P. Schneider, Eur. Phys. J. C **74**, 3180 (2014).

[15] R. Arnaldi *et al.*, Phys. Lett. B **757**, 47 (2016).

[16] T. Husek, K. Kampf, and J. Novotný, Phys. Rev. D **92**, 054027 (2015).

[17] K. Mikaelian and J. Smith, Phys. Rev. D **5**, 1763 (1972).

[18] J. R. Batley *et al.*, Phys. Lett. B **746**, 178 (2015).

[19] P. Adlarson *et al.*, Phys. Lett. B **726**, 187 (2013).

[20] G. Agakishiev *et al.*, Phys. Lett. B **731** 265 (2014).

[21] H. J. Behrend *et al.*, Z. Phys. C **49**, 401 (1991).

[22] R. Meijer Drees *et al.*, Phys. Rev. D **45**, 1439 (1992).

[23] P. Masjuan, Phys. Rev. D **86**, 094021 (2012).

[24] J. Gronberg *et al.*, Phys. Rev. D **57**, 33 (1998).

[25] P. del Amo Sanchez *et al.*, Phys. Rev. D **84**, 052001 (2011).

[26] S. Uehara *et al.*, Phys. Rev. D **86**, 092007 (2012).

[27] F. Niecknig, B. Kubis, and S. P. Schneider, Eur. Phys. J. C **72**, 2014 (2012)

[28] M. Hoferichter, B. Kubis, and D. Sakkas, Phys. Rev. D **86**, 116009 (2012).

[29] P. Aguar-Bartolome *et al.*, Phys. Rev. C **89**, 044608 (2014).

[30] H. Berghäuser *et al.*, Phys. Lett. B **701**, 562 (2011).

[31] D. Hornidge *et al.*, Phys. Rev. Lett. **111**, 062004 (2013).

[32] P. Adlarson *et al.*, Phys. Rev. C **92**, 024617 (2015).

[33] A. Starostin *et al.*, Phys. Rev. C **64**, 055205 (2001).

[34] R. Novotny, IEEE Trans. Nucl. Sci. **38**, 379 (1991).

[35] A. R. Gabler *et al.*, Nucl. Instrum. Methods Phys. Res. A **346**, 168 (1994).

[36] H. Herminghaus *et al.*, IEEE Trans. Nucl. Sci. **30**, 3274 (1983).

[37] K.-H. Kaiser *et al.*, Nucl. Instrum. Methods Phys. Res. A **593**, 159 (2008).

[38] I. Anthony *et al.*, Nucl. Instrum. Methods Phys. Res. A **301**, 230 (1991).

[39] S. J. Hall *et al.*, Nucl. Instrum. Methods Phys. Res. A **368**, 698 (1996).

[40] J. C. McGeorge *et al.*, Eur. Phys. J. A **37**, 129 (2008).

[41] S. Prakhov *et al.*, Phys. Rev. C **79**, 035204 (2009).

[42] E. F. McNicoll *et al.*, Phys. Rev. C **82**, 035208 (2010).

[43] A. Nikolaev *et al.*, Eur. Phys. J. A **50**, 58 (2014).

[44] D. Watts, Proceedings of the 11th International Conference on Calorimetry in Particle Physics, Perugia, Italy, 2004 (World Scientific, 2005) p. 560.

[45] A. Krasznahorkay *et al.*, Phys. Rev. Lett. 116 (2016) no. 4, 042501.

[46] J. L. Feng, B. Fornal, I. Galon, S. Gardner, J. Smolinsky, T. M. P. Tait and P. Tanedo, arXiv:1608.03591 [hep-ph].

[47] J. C. Martens and J. P. Ralston, arXiv:1606.06209 [hep-ph].

[48] W. J. Marciano, A. Masiero, P. Paradisi, and M. Passera, arXiv:1607.01022v1 [hep-ph].